Electronic Supplementary Material (ESI) for Materials Chemistry Frontiers.

Electronic Supplementary Information

Optimizing strong metal-support interaction on cobalt phosphide-supported Ru single atom catalyst for highly-efficient hydrogen evolution reaction

Meng Wu,[a,b] Rui Zhang,*[a] Chen Li,[a] Xue Sun,[a] Guanjie Chen,[b] Lidan Guo,[b] Kun Zheng[a] and Xiangnan Sun*[b,c]

[a]Beijing Key Laboratory of Microstructure and Property of Solids, Faculty of Materials and Manufacturing, Beijing University of Technology, Beijing 100124, China. E-mail: zhangr09409@bjut.edu.cn

[b]Key Laboratory of Nanosystem and Hierarchical Fabrication, National Center for Nanoscience and Technology, Beijing 100190, China. E-mail: sunxn@nanoctr.cn

[c]School of Material Science and Engineering, Zhengzhou University, Zhengzhou 450001, China.

Experimental Section

Materials

Ruthenium chloride ($RuCl_3 \cdot 6H_2O$, AR) was purchased from Ai Rui (Shanghai) Chemical Technology Co., LTD. $Co(NO_3)_2 \cdot 6H_2O$, ammonium fluoride (NH_4F, AR), urea (CH_4N_2O, AR), hydrochloric acid (HCl, AR), acetone (C_3H_6O, AR), ethanol (C_2H_5OH, AR), potassium hydroxide (KOH, AR) and sodium hypophosphite (NaH_2PO_2, AR) were obtained from Sinopharm Chemical Reagent Co., LTD.

Synthesis

$Ru_{SA}@CoP_x$ was prepared by a successive processes of hydrothermal synthesis, impregnation loading and low-temperature phosphidation.

Hydrothermal synthesis of Co-HT: a piece of 2×3 cm^2 nickel foam (NF) was ultrasonically treated with ethanol, deionized water and 1 M HCl for 30 minutes to remove the surface oxide layer. Then 2 mmol cobalt nitrate hexahydrate, 6 mmol ammonium fluoride, 10 mmol urea and 35 mL deionized water were added to a glass beaker (250 mL) by magnetic stirring for 20-30 min and transferred to a Teflon-lined reactor with a capacity of 50 mL. The pre-treated nickel foam was put into the solution. The sealed reactor was heated at 120 °C for 10 h and then cooled to ambient temperature. The obtained sample was washed with deionized water and anhydrous ethanol respectively before dried at 60 °C.

Preparation of Ru_{SA}@Co-HT: 2 mL $RuCl_3 \cdot 6H_2O$ stock solution at a concentration of 10 $mg \cdot mL^{-1}$ was added to a glass beaker (50 mL) and diluted to 1 $mg \cdot mL^{-1}$ with deionized water. Afterwards, the pre-synthesized Co-HT is immersed in the solution for 6 h. After impregnation, the sample was rinsed 3 times with deionized water and anhydrous ethanol, and finally dried at 60 °C to obtain Ru_{SA}@Co-HT.

Preparation of $Ru_{SA}@CoP_x$: Placing 0.3 g sodium hypophosphite monohydrate ($NaH_2PO_2 \cdot H_2O$) in the porcelain boat at the upstream of the carrier gas and a piece of Ru_{SA}@Co-HT at the downstream site. Then the porcelain boat was sealed in the quartz tube of the tubular furnace and heated to the preset temperature (300, 350 and 400 °C in this study) at a heating rate of 3 $°C \cdot min^{-1}$ under argon atmosphere and kept for 2 h.

The preparation of CoP_x was similar to that of $Ru_{SA}@CoP_x$ except that the impregnation was not used in the synthesis processes.

Characterizations

X-ray diffraction (XRD) patterns were recorded on the D/MAX 250 diffractometer, using Cu K_α radiation (λ=1.54178 Å) at 40 kV voltage and 15 mA current. The scanning speed was 4° min^{-1}. Scanning electron microscope (SEM) images were obtained by the Hitachi S-4800 field emission SEM. Transmission electron microscopy (TEM), high Angle ring dark field scanning transmission electron microscopy (HAADF-STEM), and corresponding energy dispersive X-ray spectroscopy (EDS) analyses were performed and recorded on a Tecnai G2 F20 U-TWIN transmission electron microscope equipped with an energy dispersive X-ray detector. Aberration-corrected scanning transmission electron microscopy (AC-STEM) was performed on the FEI Titan G2 Themis. X-ray photoelectron spectroscopy (XPS) was obtained by ESCALAB MK II X-ray photoelectron spectrometer using Mg K_α as the excitation source. X-ray Absorption Near-Side Structure (XANES) and Extended X-ray Absorption Fine Structure (EXAFS) images were acquired by the Singapore

Synchrotron Light Source (SSLS) Centre. The operating energy of the storage ring is 2.5 GeV and the average current is less than 200 mA. A pair of channel-cut Si (111) crystal monochromators were used to monochrome the radiation.

Electrochemical Measurements

The electrochemical performance of all samples was tested on the CHI760E electrochemical workstation using a standard three-electrode device. The working electrode was cut into 1×1 cm^2 square pieces. The counter electrode was a carbon rod, and the reference electrode was Ag/AgCl impregnated in a saturated potassium chloride solution. The electrochemical curve was measured in 1.0 M KOH and corrected to a reversible hydrogen electrode by E(vs RHE) = E(Ag/AgCl) + 0.197 V + 0.059 × pH, and $E_{iR\text{-corrected}}$ = E(vs RHE) - iR compensation resistance.

Cyclic voltammetry (CV) was firstly conducted between -600 mV to 200 mV versus RHE at a sweep rate of 100 mV s^{-1}, until they reached the steady state. The linear sweep voltammetry (LSV) curves were subsequently measured at the scanning rate of 2 mV·s^{-1}. The solution resistances were measured via impedance test. Electrochemical impedance spectra were measured at open circuit potential from 10^5 Hz to 0.1 Hz. The current density (j) was obtained by the set area normalization. The Tafel slope is obtained by linear fitting the points in the Tafel region of the LSV data. ECSA tests were measured by cyclic voltammetry at different scan rates (20 mV s^{-1}, 40 mV s^{-1}, 60 mV s^{-1},80 mV s^{-1}, 100 mV s^{-1}, 120 mV s^{-1}, 140 mV s^{-1}, 160 mV s^{-1}, 180 mV s^{-1}, 200 mV s^{-1}). The stability test was performed by chronopotentiometry (*i-t* curves at current densities of 10, 20, 30 and 50mA·cm^{-2}) and cyclic voltammetry (CV) for 1000 scans at a scanning rate of 2 mV·s^{-1}.

DFT Calculations

The total density functional theory computations were performed using the Vienna Ab initio Simulation Package (VASP), using the plane-wave pseudopotentail method with ultra-sotf pseudopotentials. The generalized gradient approximation (GGA) based on the Perdew-Burke-Erzerhof (PBE) was adopted to describe the exchange-correlation interactions. Nudged Elastic Band method of Transition State Tools for VASP was used for transition state search. We have focused on the Pt(111), CoP(200) and Co_2P(111) structure with a lattice parameter of 3.94, 5.60×5.08×3.21 and 6.61×5.65×3.51 angstrom. Integration in the Brillouin zone was performed on the basis of the Monkhorst-Pack scheme using a 5×5×1 k-point mesh in initial lattice constant optimization, a 3×3×1 k-point mesh in transition state search, and a greater than 12×12×1 k-point mesh in electronic structure calculations. The convergence criteria of energy and force were set to 10^{-5} eV and 0.01eV $Å^{-1}$ for geometry optimization, and 0.03 eV $Å^{-1}$ for transition state search. The plane-wave cutoff energy was set as 520 eV.

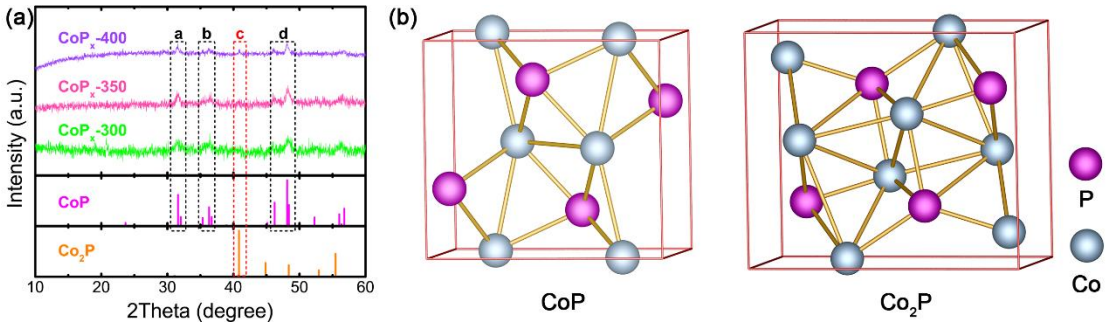

Fig. S1 (a) XRD patterns of CoP_x prepared at different temperatures along with the standard powder diffraction cards of CoP(PDF No. 29-0497) and Co_2P(PDF No. 54-0413). (b) Crystal structures of CoP and Co_2P.

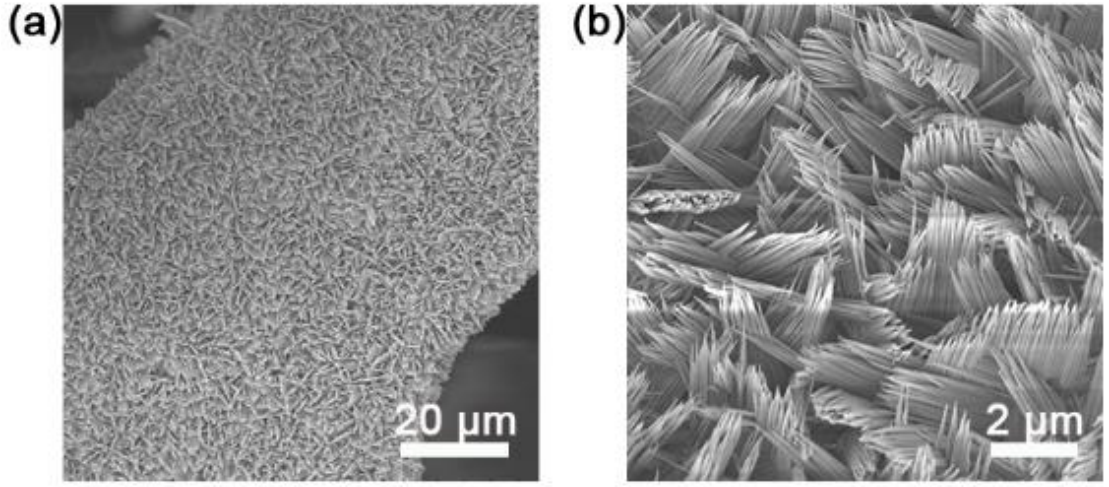

Fig. S2 SEM images of Co-HT precursor.

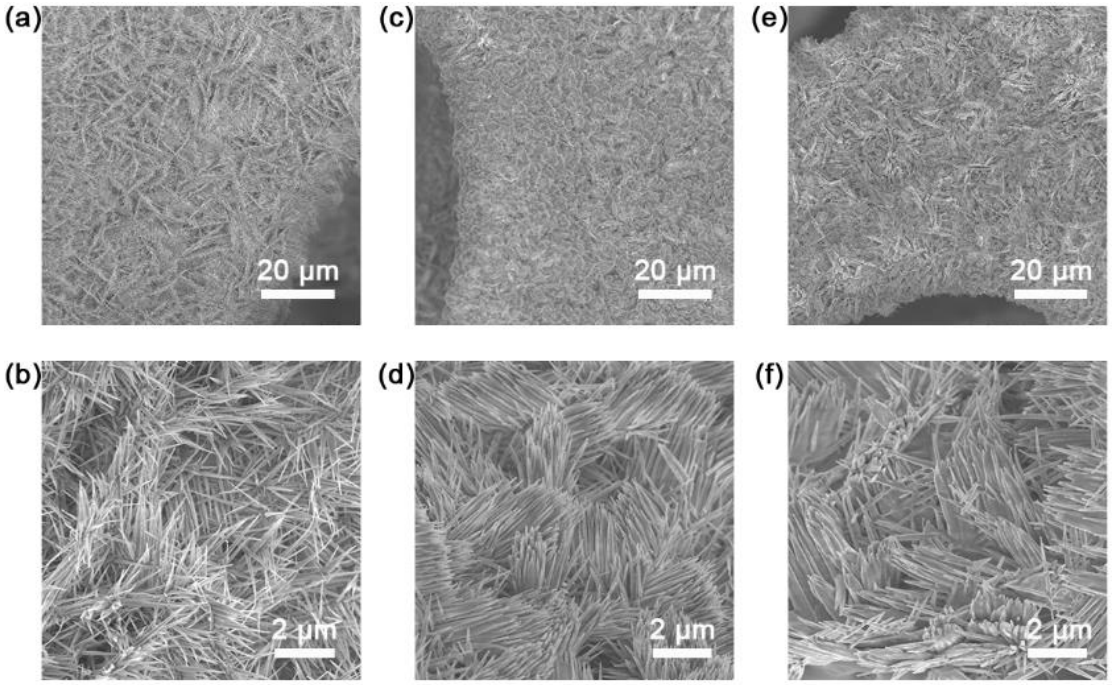

Fig. S3 SEM images of (a, b) CoP_x-300, (c, d) CoP_x-350 and (e, f) CoP_x-400.

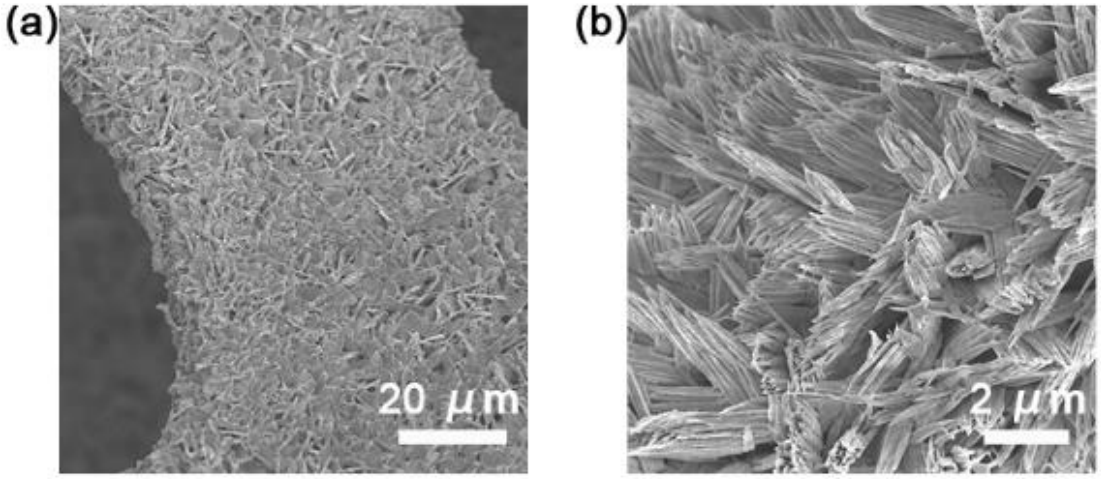

Fig. S4 SEM images of $Ru_{SA}@CoP_x$-300.

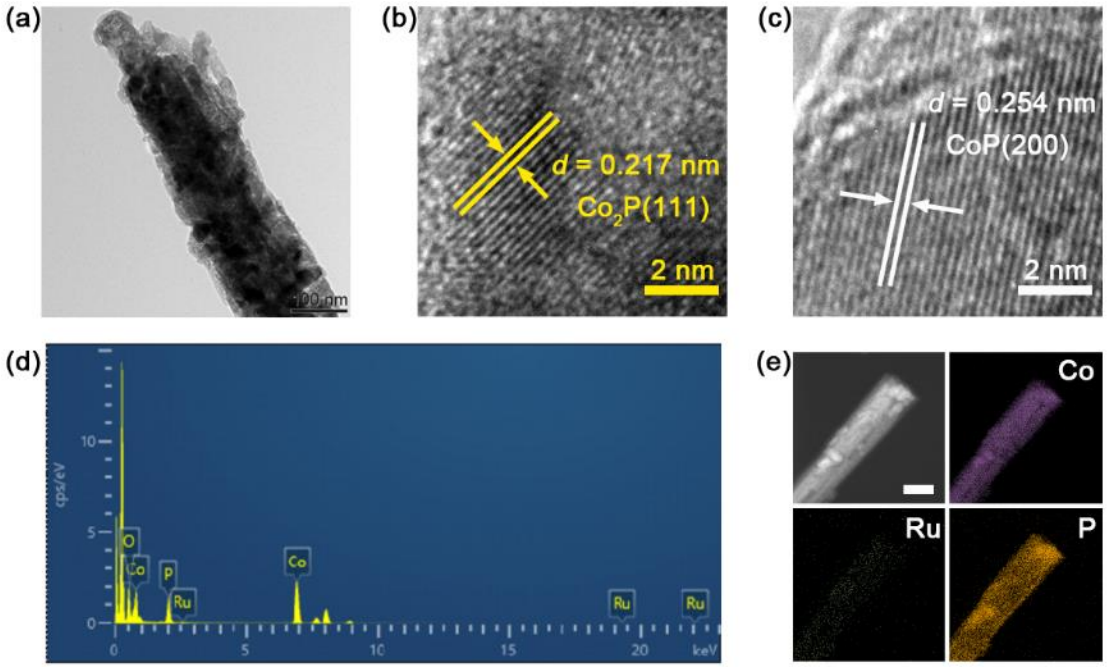

Fig. S5 TEM characterizations of $Ru_{SA}@CoP_x$-300. (a) TEM and (b, c) HR-TEM images. (d) EDS pattern. (e) HAADF-STEM elemental mappings of Co, Ru and P, the scale bar is 100 nm.

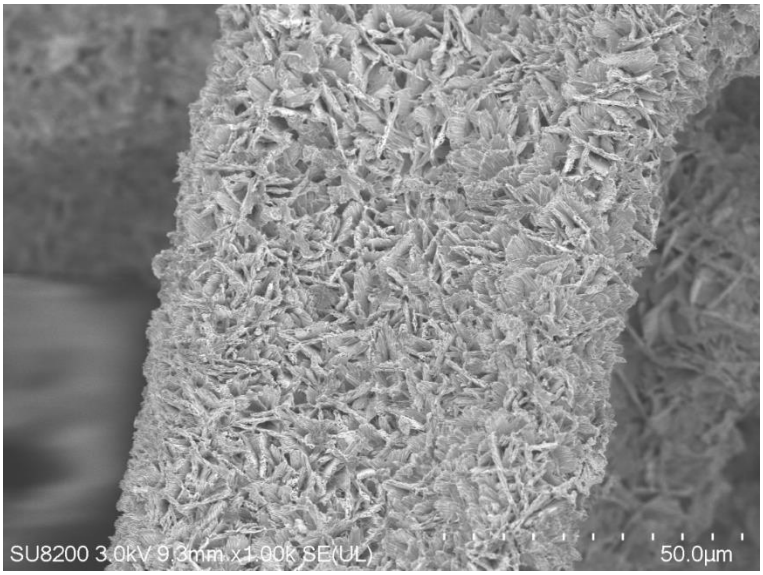

Fig. S6 SEM image of $Ru_{SA}@CoP_x$-350.

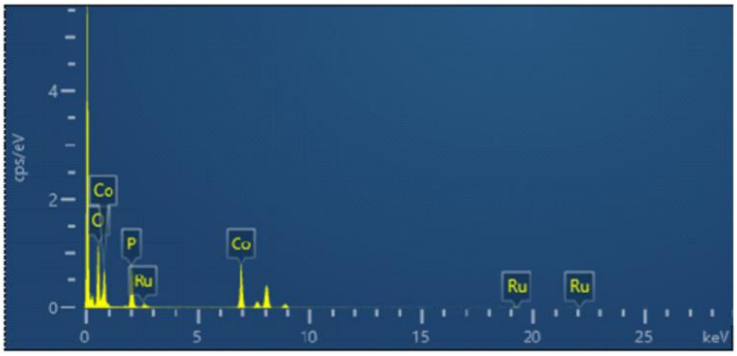

Fig. S7 EDS pattern of $Ru_{SA}@CoP_x$-350.

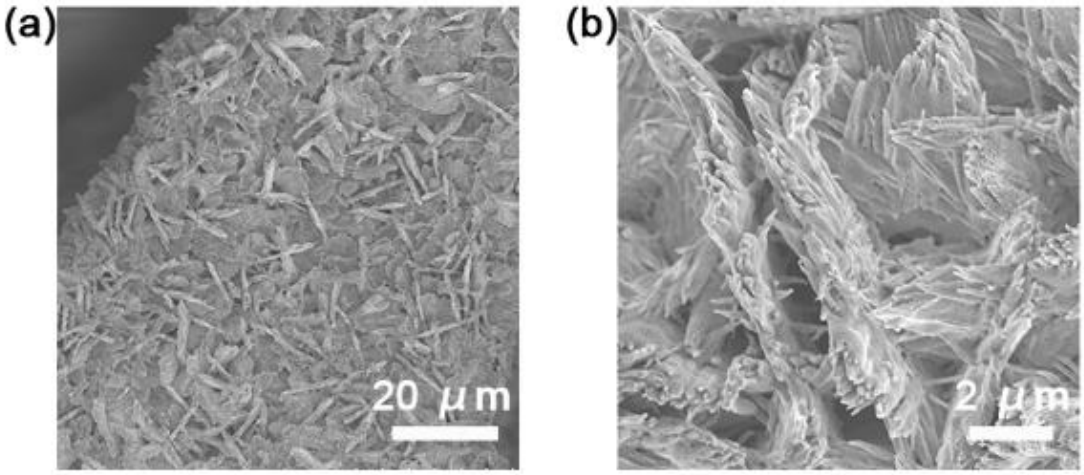

Fig. S8 SEM images of $Ru_{SA}@CoP_x$-400.

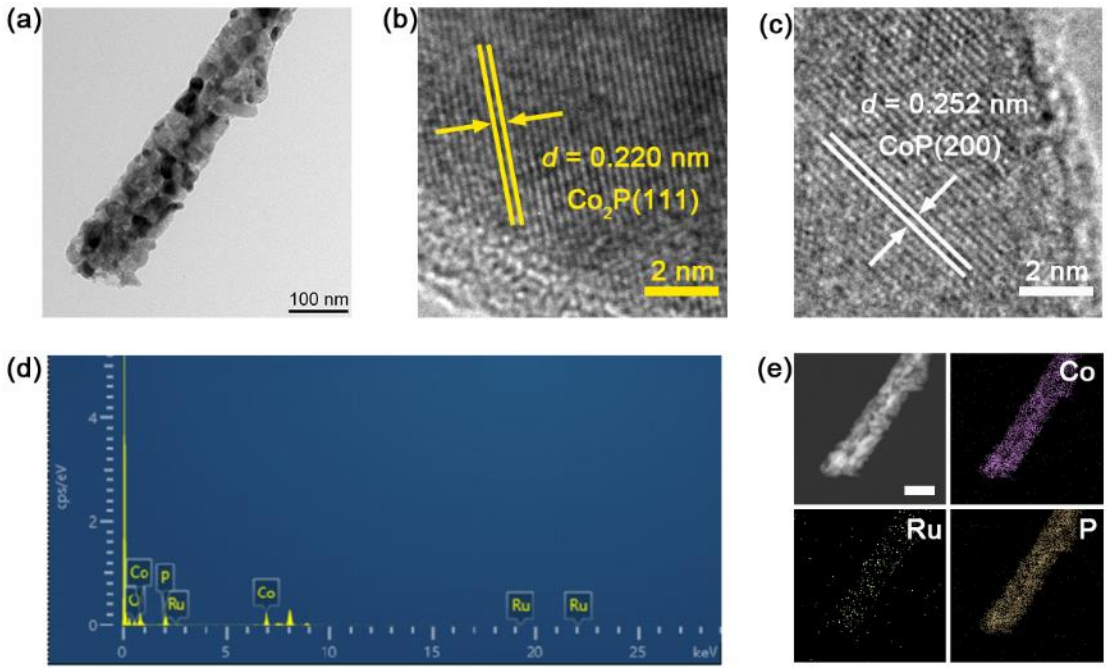

Fig. S9 TEM characterizations of $Ru_{SA}@CoP_x$-400. (a) TEM and (b, c) HR-TEM images. (d) EDS pattern. (e) HAADF-STEM elemental mappings of Co, Ru and P, the scale bar is 100 nm.

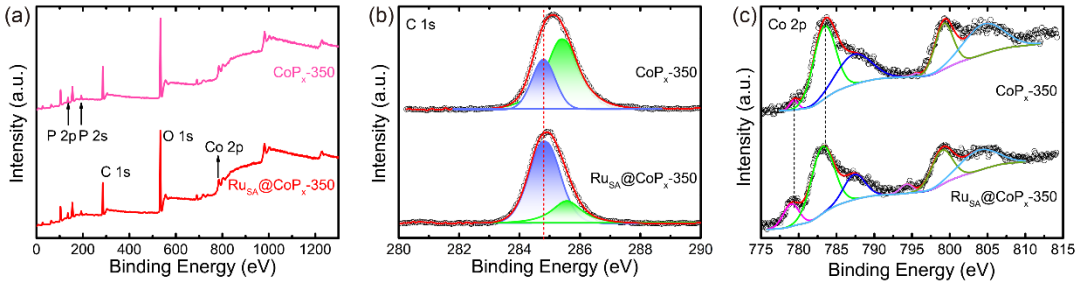

Fig. S10 XPS characterization of CoP_x-350 and $Ru_{SA}@CoP_x$-350. (a) Survey scan, (b) C 1s and (c) Co 2p spectra.

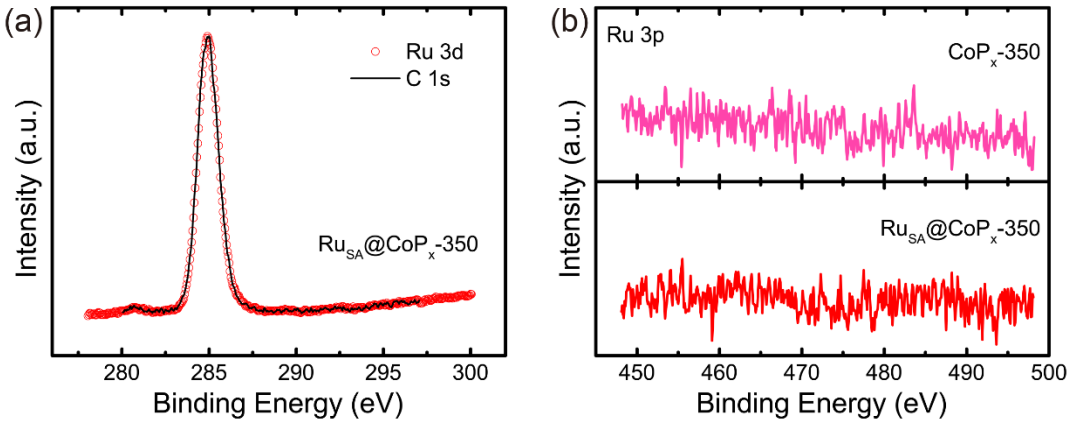

Fig. S11 (a) XPS spectra of Ru 3d along with C 1s for $Ru_{SA}@CoP_x$-350. (b) Ru 3p spectra of CoP_x-350 and $Ru_{SA}@CoP_x$-350.

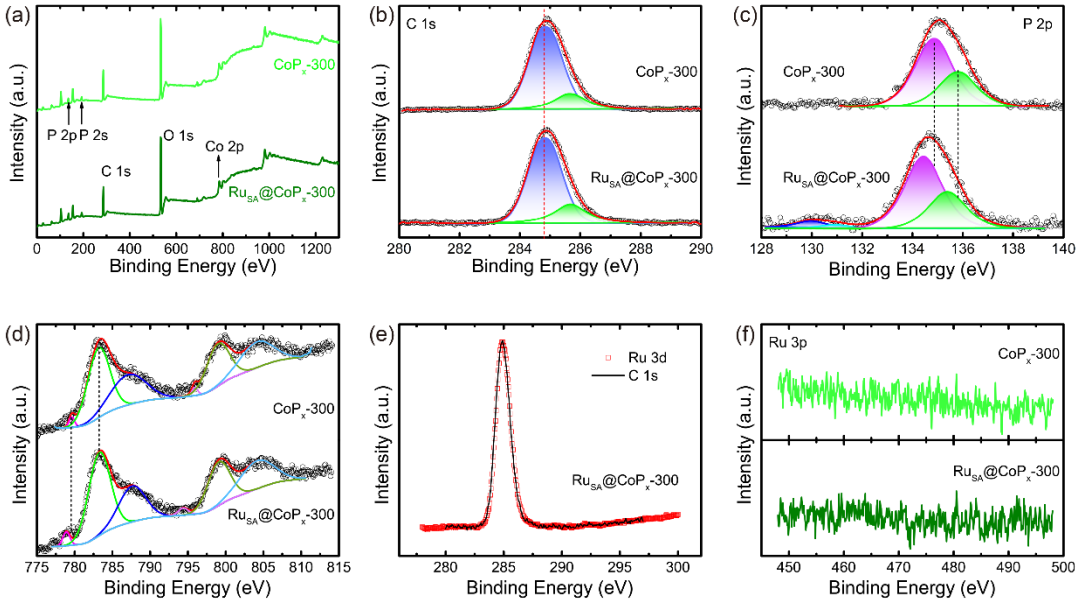

Fig. S12 XPS characterization of CoP_x-300 and Ru_{SA}@CoP_x-300. (a) Survey scan, (b) C 1s, (c) P 2p (d) Co 2p and (f) Ru 3p spectra. (e) XPS spectra of Ru 3d along with C 1s for Ru_{SA}@CoP_x-300.

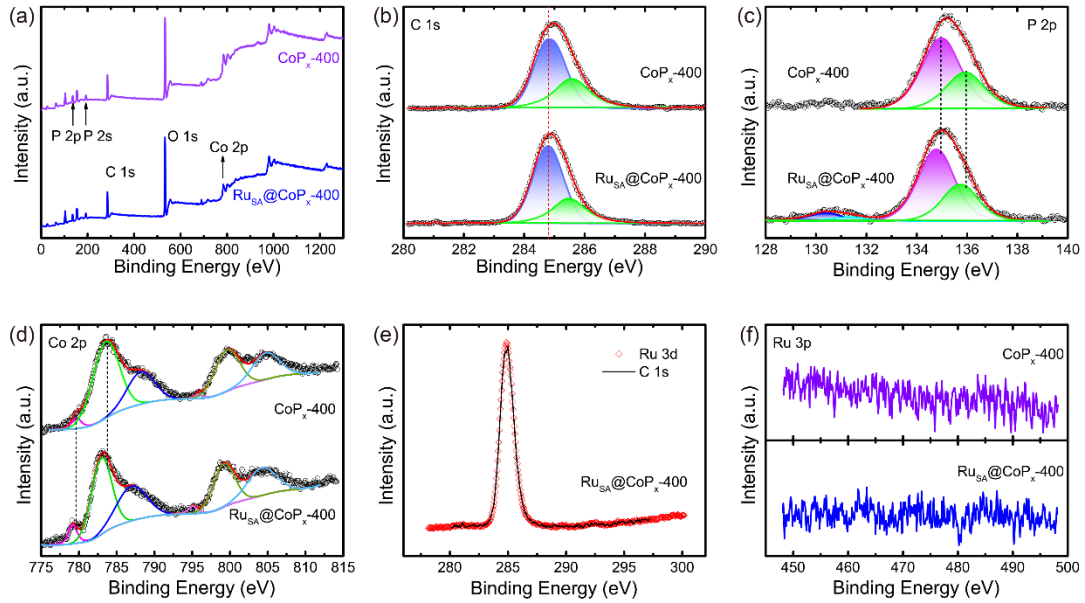

Fig. S13 XPS characterization of CoP_x-400 and Ru_{SA}@CoP_x-400. (a) Survey scan, (b) C 1s, (c) P 2p (d) Co 2p and (f) Ru 3p spectra. (e) XPS spectra of Ru 3d along with C 1s for Ru_{SA}@CoP_x-400.

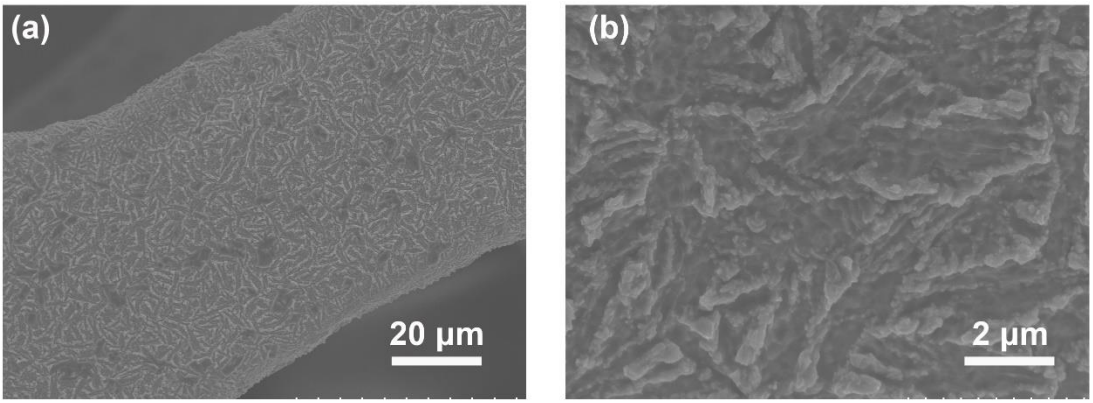

Fig. S14 SEM images of NF-P (NF phosphidated at 350 °C) under (a) low and (b) high magnification.

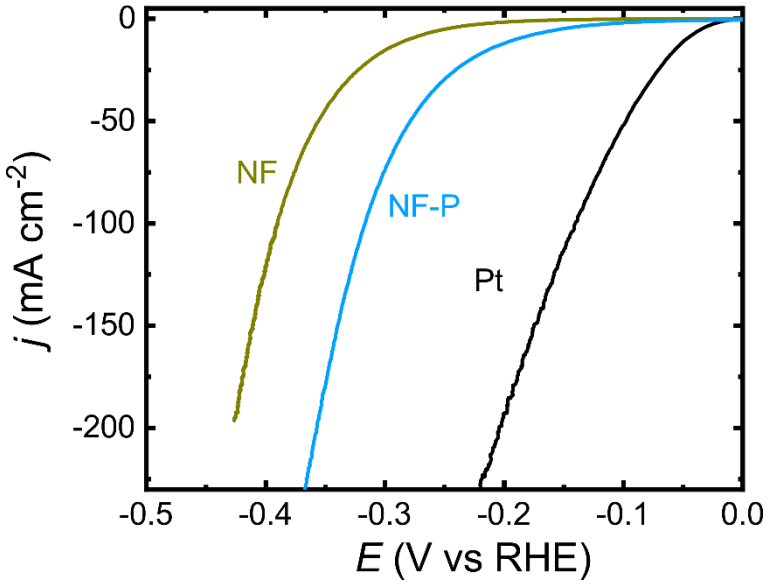

Fig. S15 LSV curves of NF, NF-P and Pt.

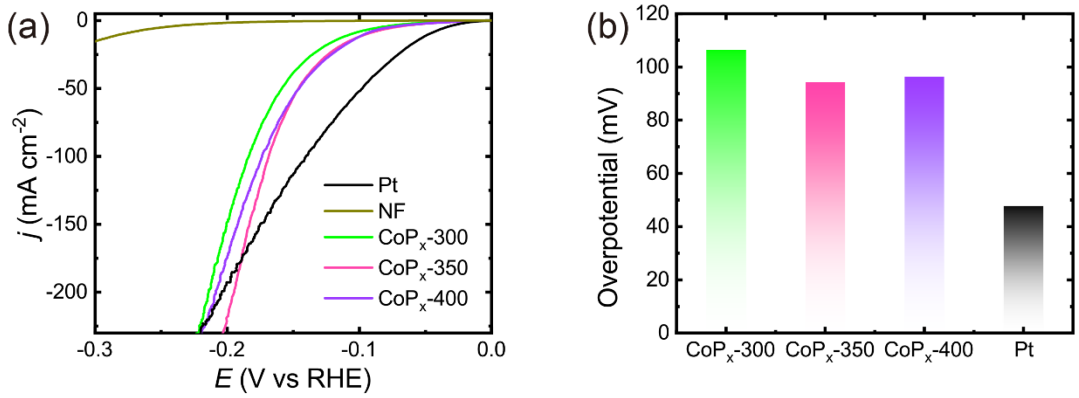

Fig. S16 (a) LSV curves of the as-prepared CoP_x-300, CoP_x-350, CoP_x-400 and commercial Pt, NF in 1 M KOH. (b) Comparison of overpotentials at the current density of 10 and 100 mA cm^{-2} for CoP_x-300, CoP_x-350, CoP_x-400 and Pt.

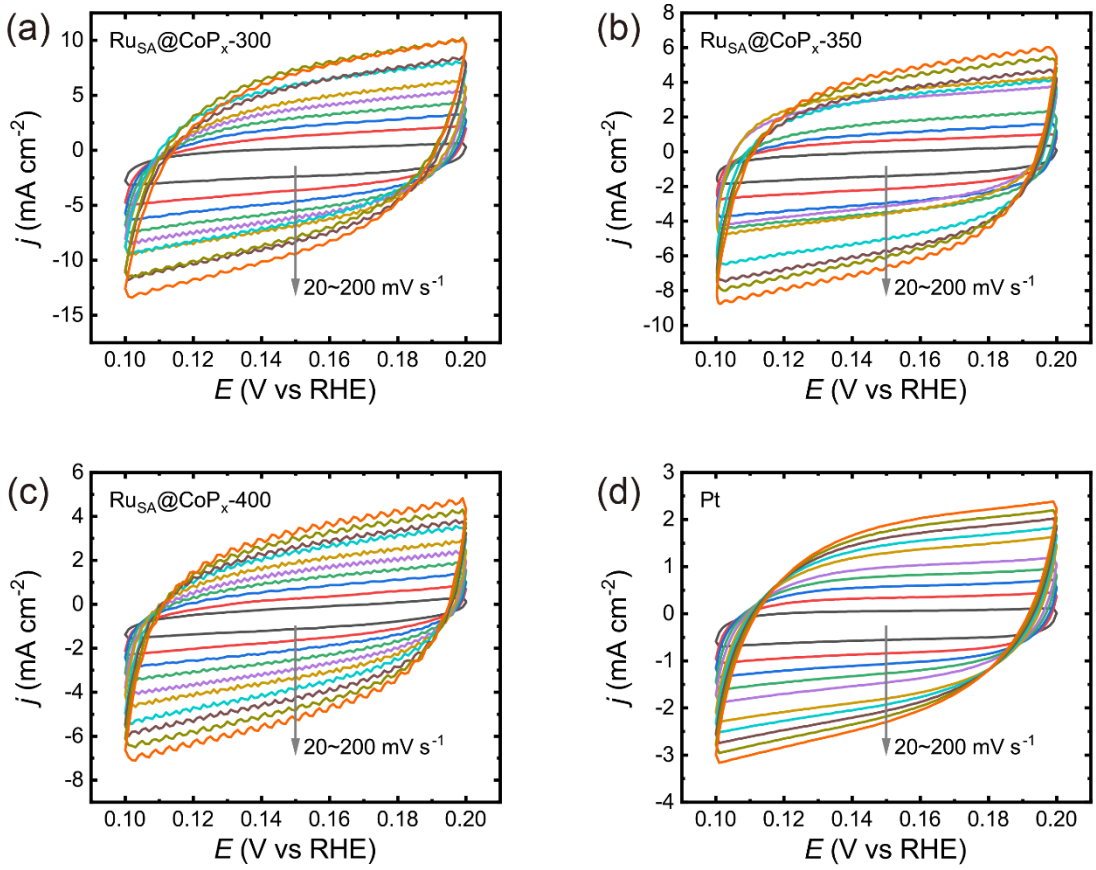

Fig. S17 Electrochemical capacitance measurements for the estimation of ECSA. Cyclic voltammograms for (a) Ru$_{SA}$@CoP$_x$-300, (b) Ru$_{SA}$@CoP$_x$-350, (c) Ru$_{SA}$@CoP$_x$-400 and (d) Pt at scan rates from 20 to 200 mV s^{-1}.

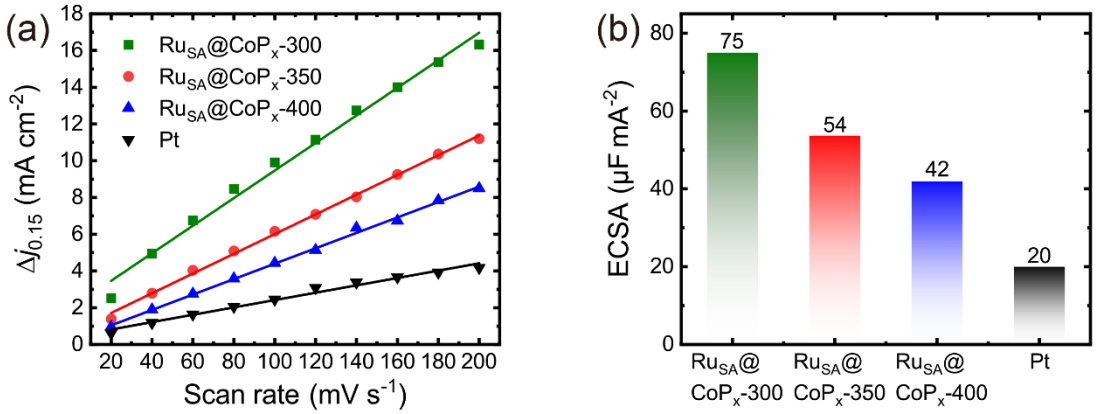

Fig. S18 (a) Capacitive currents as a function of scan rate and (b) the corresponding ECSA for Ru$_{SA}$@CoP$_x$-300, Ru$_{SA}$@CoP$_x$-350, Ru$_{SA}$@CoP$_x$-400 and Pt.

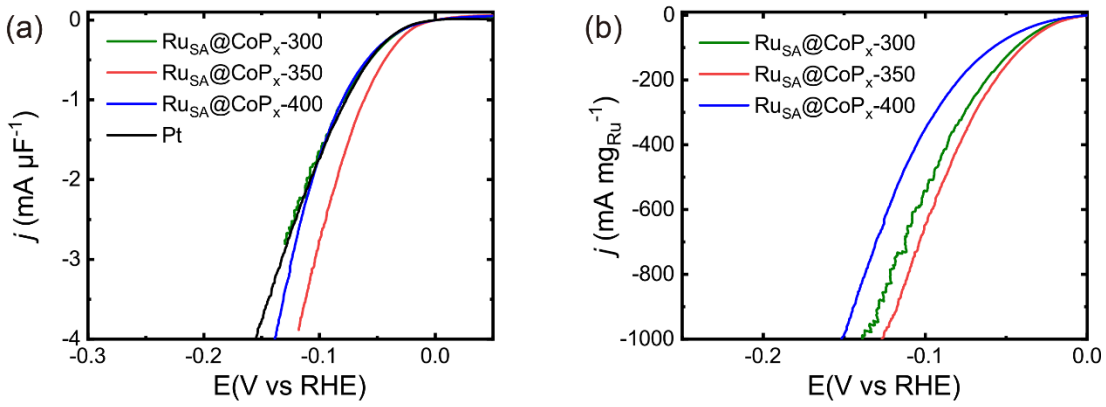

Fig. S19 Normalized HER LSV curves by (a) ECSA and (b) Ru mass.

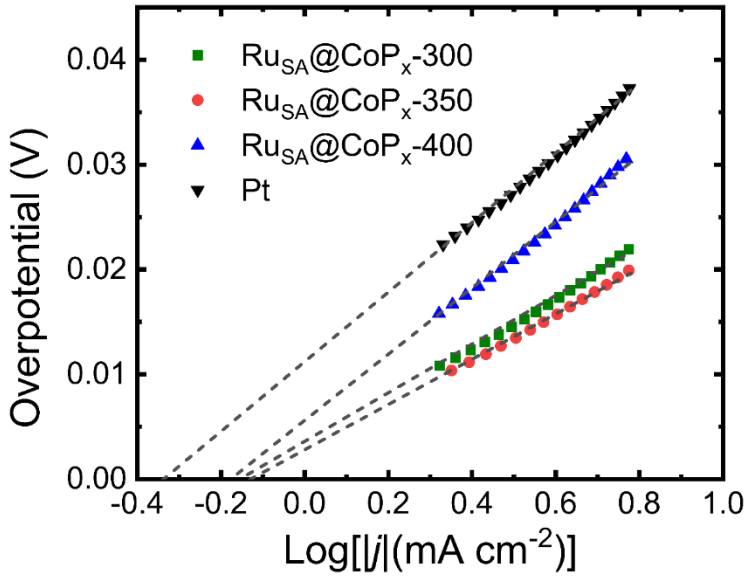

Fig. S20 Extraction of the exchange current density by the linear extrapolation.

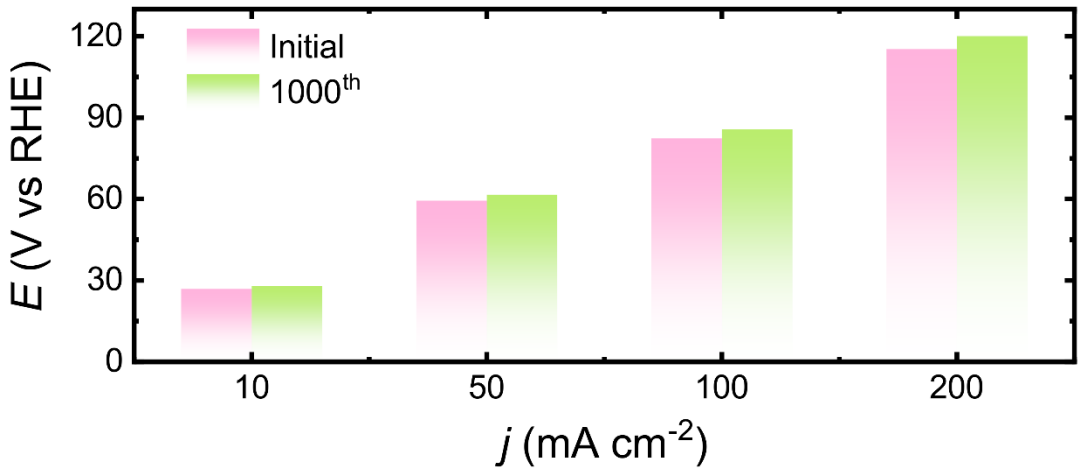

Fig. S21 Overpotentials for the initial and after 1000th CV cycling of $Ru_{SA}@CoP_x$-350 at current densities of 10, 50, 100 and 200 mA cm^{-2}.

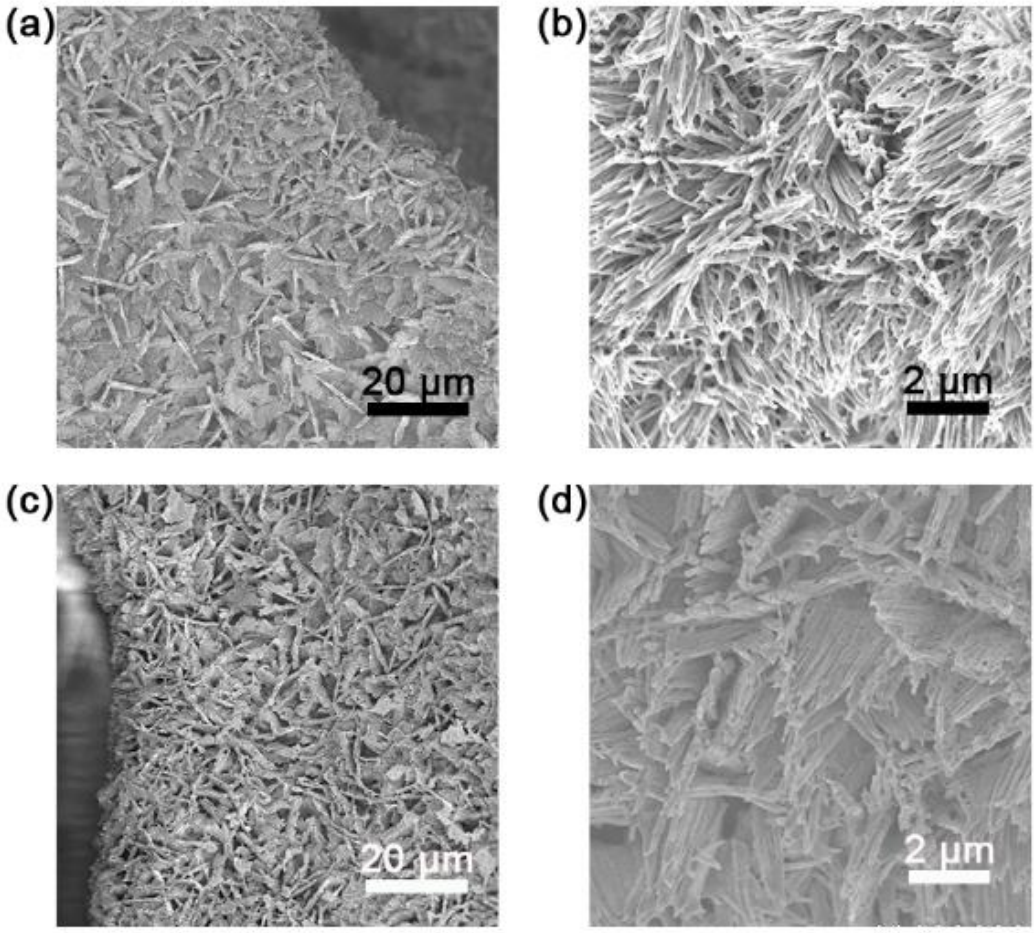

Fig. S22 SEM images of $Ru_{SA}@CoP_x$-350 at (a, b) initial and (c, d) after stability test stages.

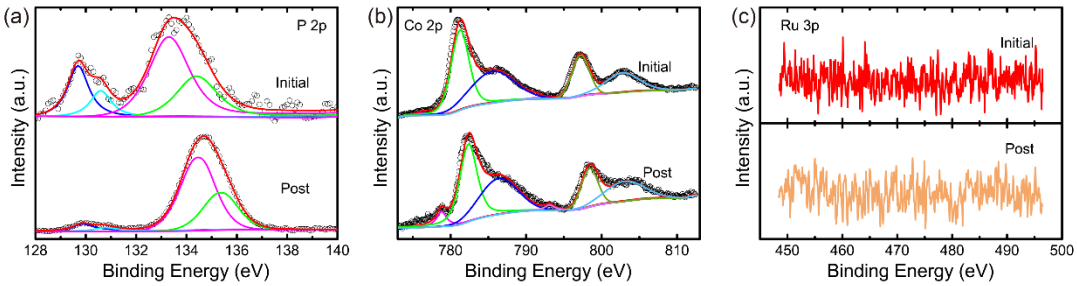

Fig. S23 XPS studies for $Ru_{SA}@CoP_x$-350 at initial and after stability test stages. (a) P 2p, (b) Co 2p and (c) Ru 3p spectra.

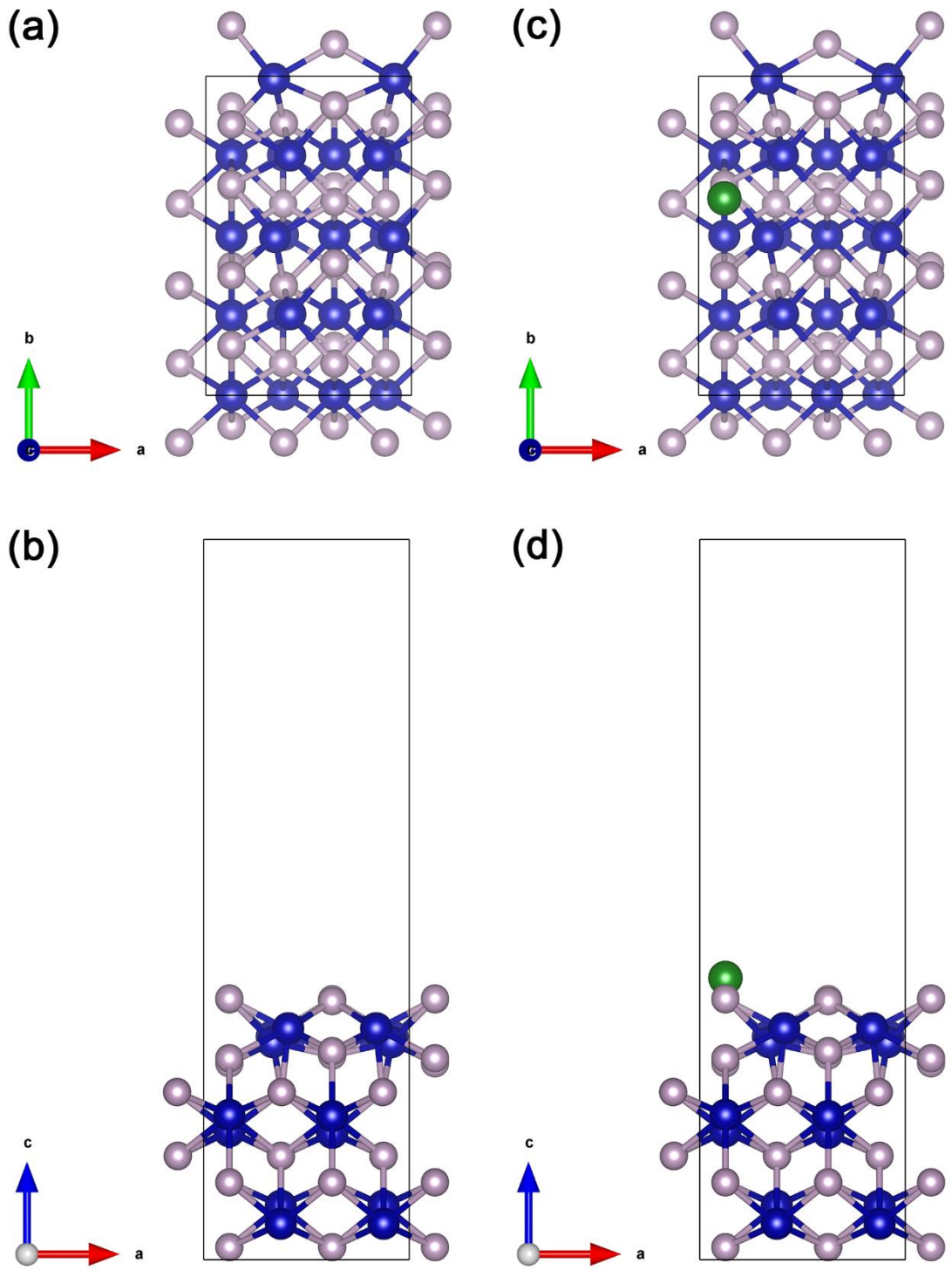

Fig. S24 Configurations of (a, b) CoP(200) and (c, d) Ru-CoP(200). The blue, green and pink spheres represent the Co, Ru and P atoms, respectively.

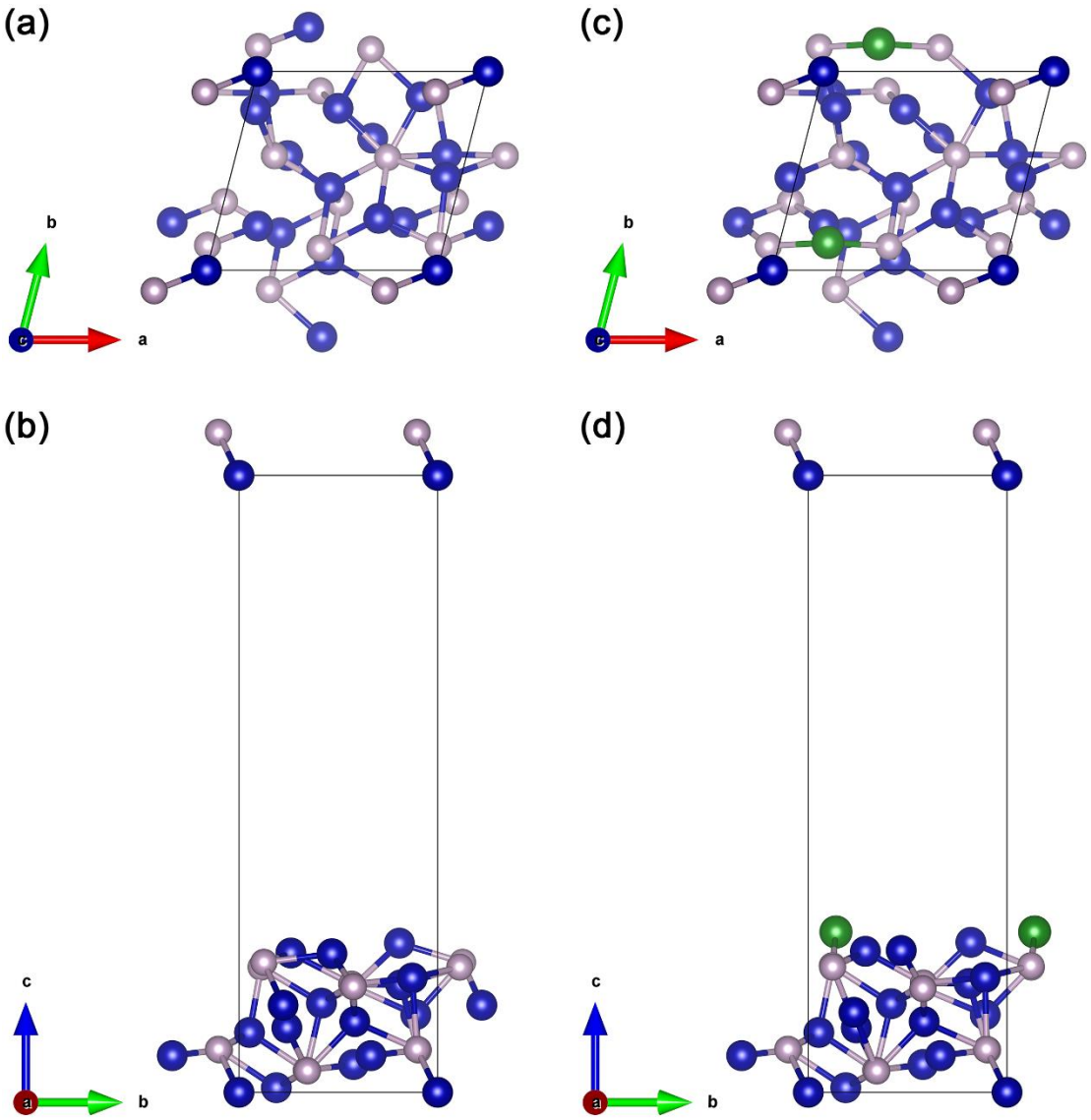

Fig. S25 Configurations of (a, b) $Co_2P(111)$ and (c, d) Ru-$Co_2P(111)$. The blue, green and pink spheres represent the Co, Ru and P atoms, respectively.

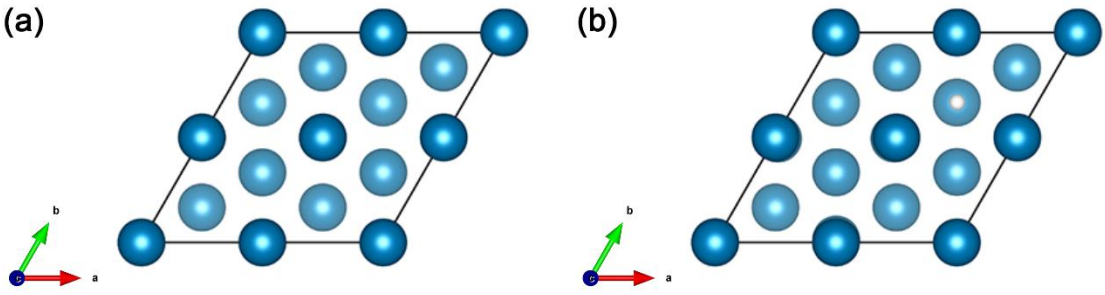

Fig. S26 Configurations of (a) Pt(111) and (b) H* on Pt(111). The cyan and white spheres represent the Pt and H atoms, respectively.

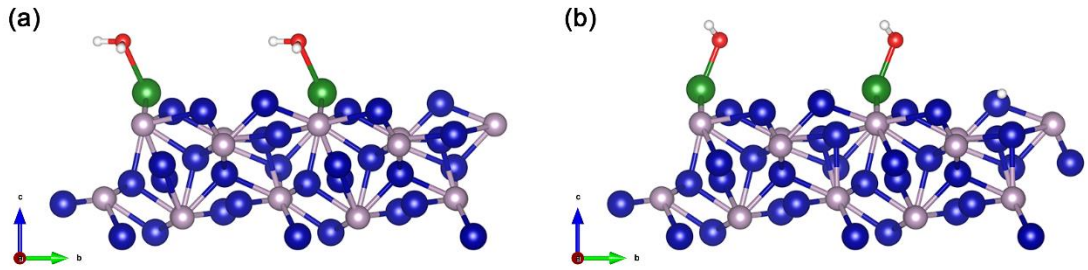

Fig. S27 The adsorption configurations of (a) H_2O* and (b) HO*+H*on the Ru-Co_2P(111). The blue, green, pink, red and white spheres represent the Co, Ru, P, O and H atoms, respectively.

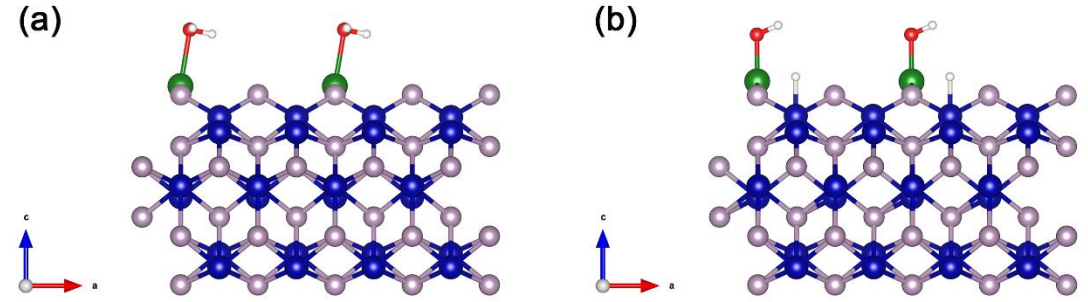

Fig. S28 The adsorption configurations of (a) H_2O* and (b) HO*+H* on the Ru-CoP(200). The blue, green, pink, red and white spheres represent the Co, Ru, P, O and H atoms, respectively.

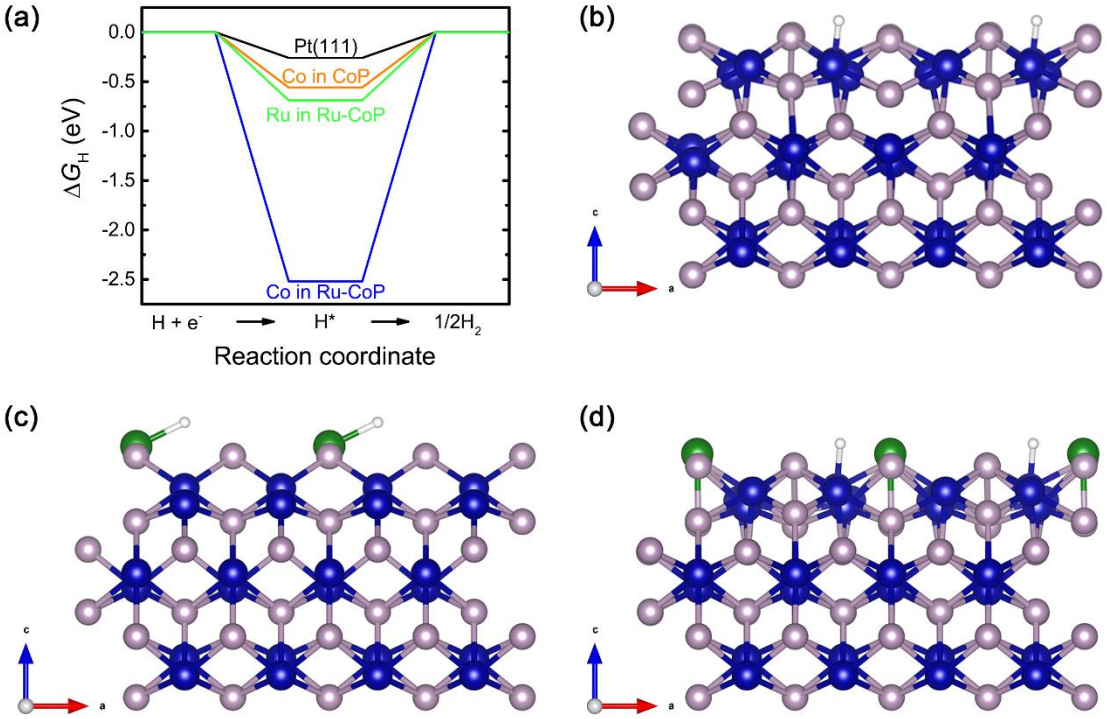

Fig. S29 (a) Calculated Gibbs-energy diagram of HER at the equilibrium potential (U_{RHE} = 0 V) for Pt(111), CoP(200) and Ru-CoP(200). The adsorption configurations of H* on the (b) Co site in CoP(200), (c) Ru site and (d) Co site (down) in Ru-CoP(200). The blue, green, pink and white spheres represent the Co, Ru, P and H atoms, respectively.

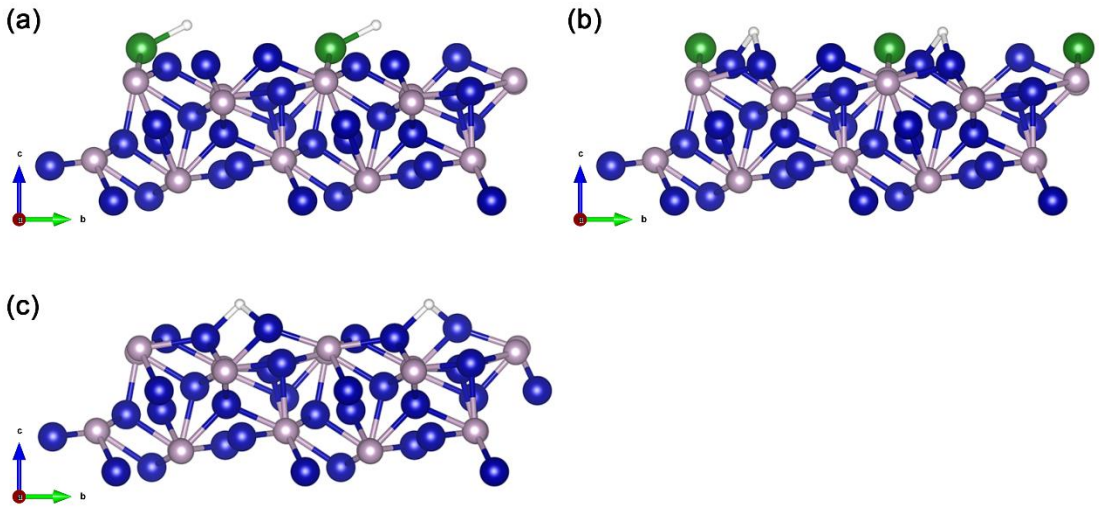

Fig. S30 The adsorption configurations of H* on the (a) Ru site and (b) Co site (down) in Ru-Co_2P(111) and (c) Co site in CoP(200). The blue, green, pink and white spheres represent the Co, Ru, P and H atoms, respectively.

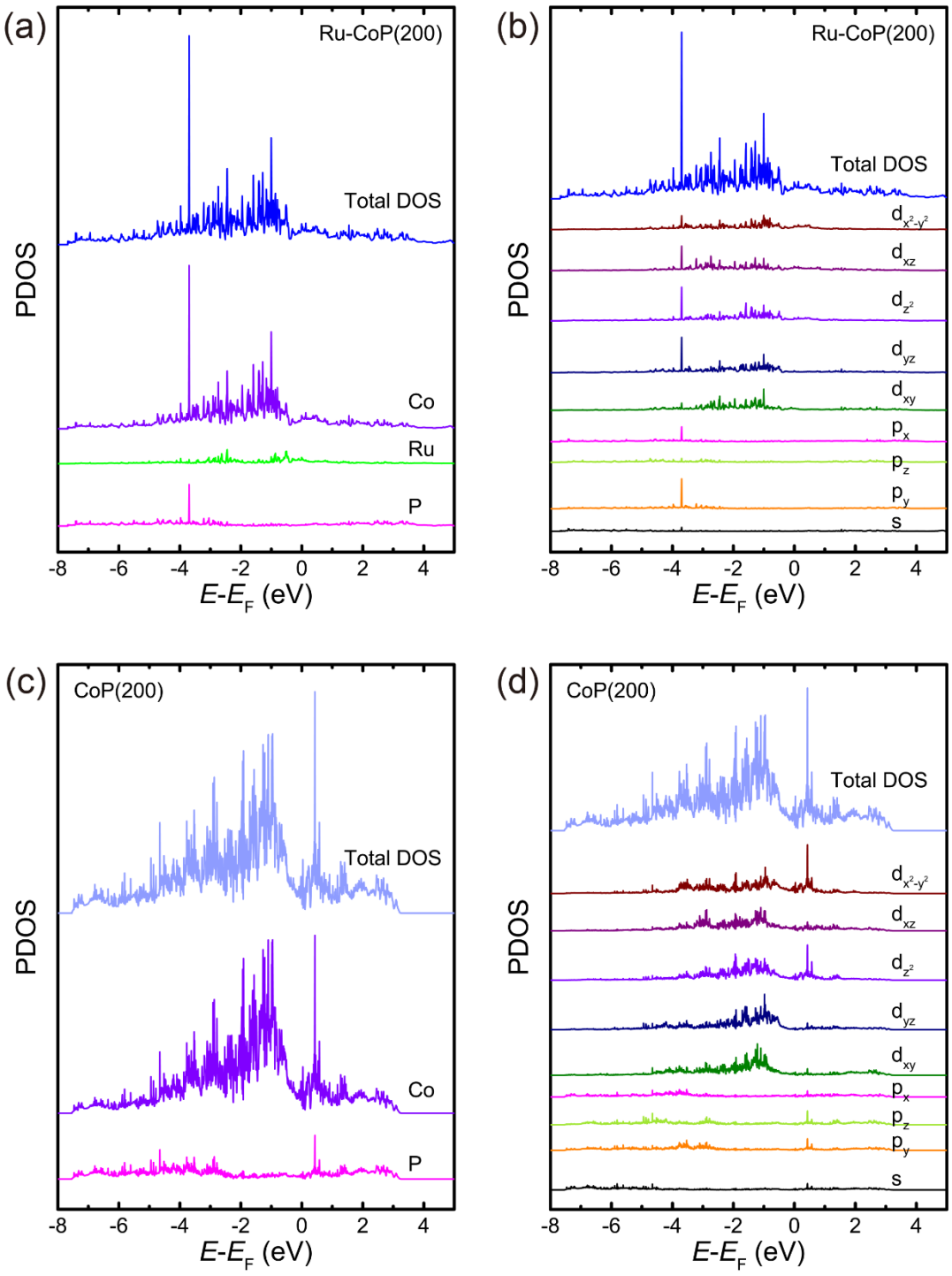

Fig. S31 PDOS for (a, b) Ru-CoP(200) and (c, d) CoP(200).

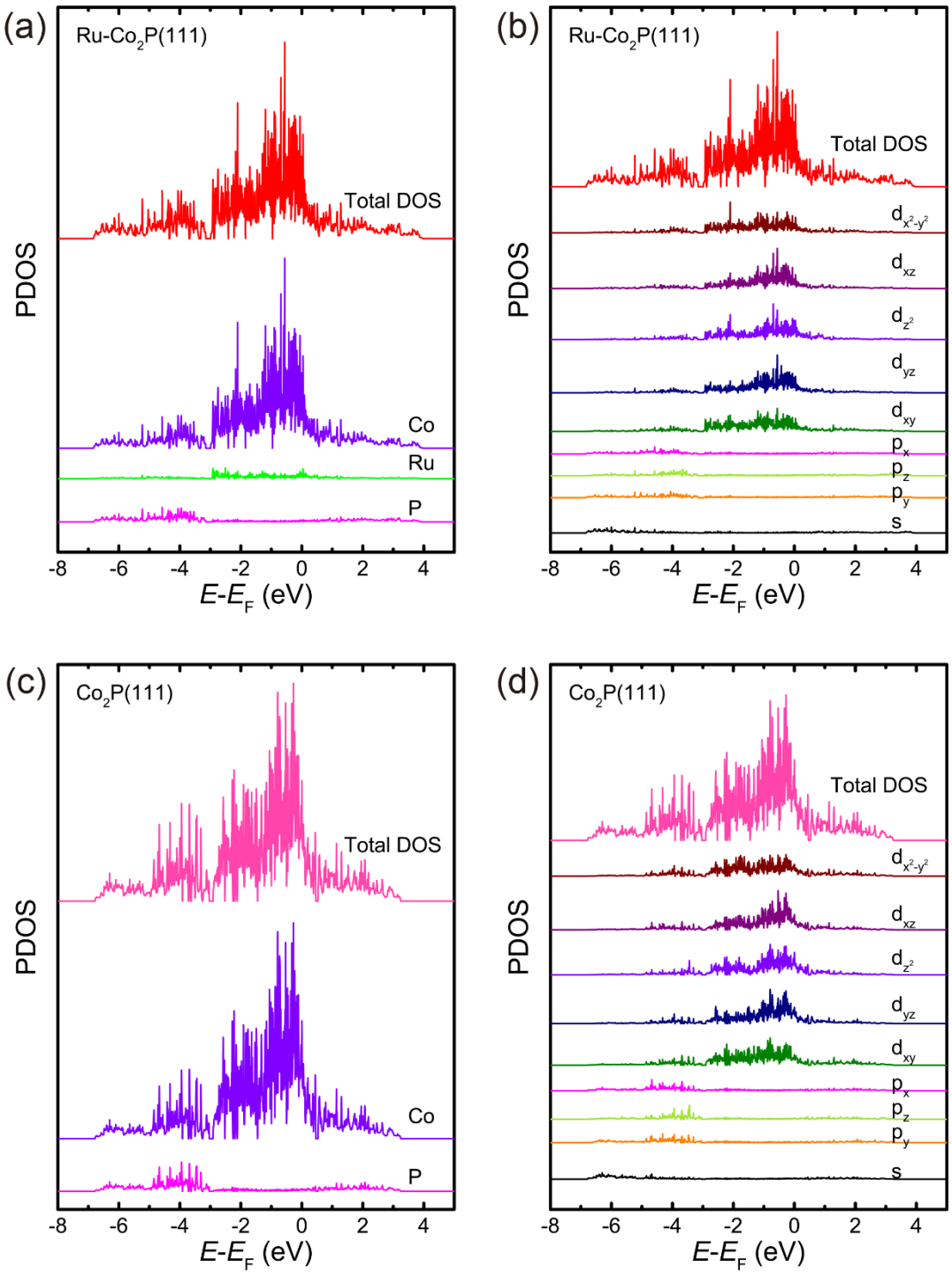

Fig. S32 PDOS for (a, b) Ru-Co_2P(111) and (c, d) Co_2P(111).

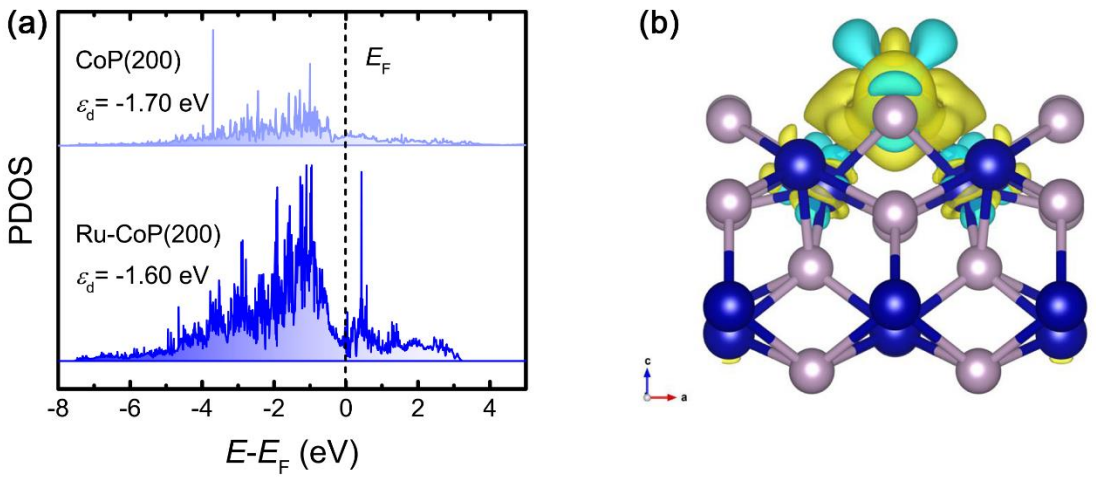

Fig. S33 (a) Partial density of states (PDOS) and d-band center values for CoP(200) and Ru-CoP(200). (b) Difference of charge density for Ru-CoP(200) with the isosurface is 0.005 e bohr^{-3}. The electron accumulation and electron depletion is marked by yellow and cyan shadows, respectively.

Table S1. The content of Ru in the $Ru_{SA}@CoP_x$. The measurement is conducted by Inductively Coupled Plasma Optical Emission Spectrometry (ICP-OES) on an Agilent ICPOES730.

Sample	Ru content (wt.%)
$Ru_{SA}@CoP_x$-300	1.48
$Ru_{SA}@CoP_x$-350	1.62
$Ru_{SA}@CoP_x$-400	1.49

Table S2. Fitting results of FT-EXAFS curves shown in Fig. 2. Herein, "Shell" is the bonding type, "CN" is the coordination number of Ru atom, "R" (Å) is the fitting bonding length, "σ^2" represents the Debye-Waller factor, and "R-factor" is used to evaluate the quality of the fitting results.

Sample	Shell	CN	R ± Δ R	σ^2	R-factor
Ru foil	Ru-Ru	6	2.67 ± 0.027	0.00364	0.024
RuO_2	Ru-O	5.7	1.98 ± 0.003	0.00291	0.018
$Ru_{SA}@CoP_x$-350	Ru-P	2.3	2.21 ± 0.076	0.01975	0.007

Table S3. The HER activity of recently reported Ru-based single atom catalysts and Ru particle catalysts in alkaline medium.

Catalyst	η_{10} (mV)	Tafel slope (mV dec^{-1})	Ref.
R-NiRu	16	40	*Adv. Mater*. **2021**, *33*, 2104764
Ru_1/D-NiFe LDH	18	29	*Nat. Commmun.* **2021**, *12*, 4587
Ru/Co-N-C	19	27.8	*Adv. Mater*. **2022**, *34*, 2110103
Ru_{SA}@CoP_x-350	26	21.6	**This work**
Ru/np-MoS_2	30	31	*Nat. Commmun.* **2021**, *12*, 1687
CC@WS_2/Ru-450	32.1	53.2	*Adv. Funct. Mater*. **2022**, *32*, 2109439
$NiRu_{0.13}$-BDC	34	32	*Nat. Commmun.* **2021**, *12*, 1369
Ru_{SA}@$Ti_3C_2T_x$	40.3	90	*EcoMat.* **2023**, *5*, e12274
Ru SAs/N-Mo_2C NSs	43	38.67	*Appl. Catal. B* **2020**, *277*, 119236
CC@MoS_2/MoP/Ru-450	45	52.9	*Chem. Eng. J.* **2021**, *414*, 128834
Ru_1CoP/CDs	51.6	73.4	*Angew. Chem. Int. Ed*. **2021**, *60*, 7234
Ni_5P_4-Ru	54	52	*Adv. Mater*. **2020**, *32*, 1906972
Ru SAs–Ni_2P	57	75	*Nano Energy* **2021**, *80*, 105467
RuSA/NSG	57.3	56.5	*Sci. China Chem*. **2022**, *65*, 611
Ru-g-CN	75.5	63.5	*Appl. Catal. B* **2022**, *310*, 121318
SA-Ru-MoS_2	76	21	*Small Methods* **2019**, *3*, 1900653
Ru-NPC	78	68.3	*Research* **2020**, *2020*, 5860712
$Ru_{1,n}$-NC	14.8	22.3	*Adv. Mater*. **2022**, *34*, 2110604
Ru_{1+NPs}/N-C	39	27.6	*ACS Appl. Mater. Interfaces* **2022**, *14*, 15250
Ru_{NP}@RuN_x-OFC/NC	19	35	*Appl. Catal. B* **2022**, *307*, 121193
Ru-CoP/NC	22	50	*ACS Appl. Mater. Interfaces* **2021**, *13*, 56035
Ru/α-MoC	25	32	*Appl. Catal. B* **2022**, *318*, 121867
P,Mo-Ru@PC	21	21.7	*Adv. Energy Mater*. **2022**, *12*, 2200029
v_s-Ru-Ni_9S_8	94	69.8	*Appl. Catal. B* **2022**, *310*, 121356
Ru@F-Ni_3N	36	52.6	*ACS Appl. Mater. Interfaces* **2022**, *14*, 36688